Comparing the Role of Floe Breakage and Melt on Summer Sea Ice Loss

Moncada, Rigoberto; Gupta, Mukund; Thompson, Andrew F.; Andrade, Jose E.

DOI
10.1029/2024JC021223

Publication date
2025

Document Version
Final published version

Published in
Journal of Geophysical Research: Oceans

Citation (APA)
Moncada, R., Gupta, M., Thompson, A. F., & Andrade, J. E. (2025). Comparing the Role of Floe Breakage and Melt on Summer Sea Ice Loss. *Journal of Geophysical Research: Oceans*, *130*(4), Article e2024JC021223. https://doi.org/10.1029/2024JC021223

JGR Oceans

RESEARCH ARTICLE
10.1029/2024JC021223

Comparing the Role of Floe Breakage and Melt on Summer Sea Ice Loss

Rigoberto Moncada[1,2], Mukund Gupta[1,3], Andrew F. Thompson[1], and Jose E. Andrade[1]

[1]California Institute of Technology, Pasadena, CA, USA, [2]Lawrence Livermore National Laboratory, Livermore, CA, USA, [3]Delft University of Technology, Delft, The Netherlands

Key Points:

- A discrete element sea ice model with stochastic breakage and thermodynamic coupling to an ocean is used to explore summer melt processes
- In a simulation fit to Baffin Bay observations, breakage and melt make similar contributions to the mass loss of floes (diameter > 2 km)
- Floe size distribution tendency is dominated by breakage for larger floes (D >21 km) and lateral melt for smaller floes (D = 2–21 km)

Supporting Information:

Supporting Information may be found in the online version of this article.

Correspondence to:

J. E. Andrade,
jandrade@caltech.edu

Citation:

Moncada, R., Gupta, M., Thompson, A. F., & Andrade, J. E. (2025). Comparing the role of floe breakage and melt on summer sea ice loss. *Journal of Geophysical Research: Oceans*, *130*, e2024JC021223. https://doi.org/10.1029/2024JC021223

Received 19 APR 2024
Accepted 18 FEB 2025

Author Contributions:

Conceptualization: Rigoberto Moncada, Andrew F. Thompson, Jose E. Andrade
Data curation: Rigoberto Moncada
Formal analysis: Rigoberto Moncada, Mukund Gupta
Funding acquisition: Andrew F. Thompson, Jose E. Andrade
Investigation: Rigoberto Moncada
Methodology: Rigoberto Moncada, Mukund Gupta, Andrew F. Thompson, Jose E. Andrade
Project administration: Andrew F. Thompson, Jose E. Andrade
Software: Rigoberto Moncada, Jose E. Andrade
Supervision: Andrew F. Thompson, Jose E. Andrade
Validation: Rigoberto Moncada, Mukund Gupta
Visualization: Rigoberto Moncada
Writing – original draft: Rigoberto Moncada, Mukund Gupta

Abstract Marginal ice zones are composed of individual sea ice floes, whose breakage and melt influence its dynamical behavior. These processes are not well represented by global or regional climate models due to the continuum approximations and uncertainties regarding forcing, data resolution and parameterizations used for sea ice. Here, we use a Discrete Element Model (DEM) coupled to a slab thermodynamic ocean to investigate how breakage and melt processes impact the decay of summer sea ice. The DEM is calibrated using MODIS satellite imagery and reanalysis data within the Arctic Ocean's Baffin Bay during June–July 2018. The sensitivity of the sea ice decay is evaluated by varying the solar heating, the ice/ocean heat exchange parameter, and a prescribed floe breakage rate. For the parameter regime that best fits observations, the ratio of mass loss of resolved floes (diameter >2 km) due to breakage versus melt is 0.47, and oceanic versus solar melt is 0.46. The rate at which resolved floes lose mass is most sensitive to the breakage rate, as compared to the solar and oceanic melt parameters. The number decay of the largest floes (D >21 km) is controlled by breakage, whereas the decay of smaller floes (D = 2–21 km) depends strongly on lateral and basal melt. Inferences from this exploration of the parameter space may help motivate more accurate parameterizations of the floe size distribution evolution in climate models.

Plain Language Summary Over the last 40 years, the Arctic Ocean has experienced significant reduction in the areal extent and thickness of its summertime sea ice. These changes are largely occurring over marginal ice zones, located between the consolidated sea ice and open ocean, where ice is most vulnerable to melt from the ocean and atmosphere. Simulations of marginal ice zone physics are currently limited, as they do not resolve complex interactions between individual sea ice floes. Here, we use a model that simulates 2-D floes to study the summer months in Baffin Bay, a region located west of Greenland. We explore the sensitivity of sea ice loss to fracturing as well as ocean and solar heat exchanges. In the parameter regime that best agrees with satellite observations, we find that breakage and melt both play an important role in the decline of sea ice. The largest floes, with a diameter greater than approximately 21 km, are more sensitive to breakage, whereas smaller floes respond strongly to melt. Our exploration of a range of environmental conditions may help extend our conclusions to other sea ice regions governed by different regimes.

1. Introduction

In the last few decades, sea ice in the Arctic Ocean has experienced a significant decline in areal concentration, multi-year ice fraction, and thickness (Deser et al., 2010; Moon & Thoman, 2021; Serreze & Stroeve, 2015a; Stroeve et al., 2014). This decrease in sea ice cover has led to a longer ice-free season (Kwok et al., 2004; Min et al., 2021; Tooth & Tschudi, 2018; Wei et al., 2019), with ice albedo feedback being one of the contributors to greater absorption of solar heating. These summertime changes in sea ice are not well captured by climate models and are challenging to forecast (Andersson et al., 2021; Blanchard-Wrigglesworth et al., 2015; Guemas et al., 2016; Olonscheck et al., 2019; Serreze & Stroeve, 2015b). One of the factors that may limit predictions is the difficulty in capturing small-scale sea ice physics including the fracture and melt of individual floes in response to exchanges with the ocean and atmosphere. These floe-scale breakage and melt processes can strongly affect the state of the pack in both polar regions.

The floe-like behavior of sea ice has been investigated from aerial and satellite imagery, which report on floe size distribution (FSD), typically characterized by a power law relationship (Denton & Timmermans, 2022; Horvat et al., 2019; Rothrock & Thorndike, 1984; Steele, 1992; Stern, Schweiger, Stark, et al., 2018). The exponent of this power law, α, varies seasonally, with a shallower slope (more large floes) in winter and a steeper slope (more

Writing – review & editing: Rigoberto Moncada, Mukund Gupta, Andrew F. Thompson, Jose E. Andrade

small floes) in summer (Stern, Schweiger, Stark, et al., 2018). During the spring-to-summer transition, floe breakage due to waves, floe collisions and melt fractures can steepen the FSD, whereas vertical and lateral melt can cause a shoaling of the FSD as they preferentially melt smaller floes (Hwang & Wang, 2022; Stern, Schweiger, Stark, et al., 2018). Breakage and melt processes are also coupled, since smaller floes tend to be more prone to lateral melt (Gupta & Thompson, 2022; Horvat et al., 2016; Perovich & Jones, 2014; Steele, 1992), and thinner sea ice is more susceptible to fragmentation due to melt ponds and other weaknesses within the ice (Hwang et al., 2017; Ren et al., 2021). Simulating sea ice breakage is a challenging task, owing to the diverse fracture mechanisms that play a role, including those induced by winds (Dempsey et al., 1994; Dinh et al., 2023; Lu et al., 2015; Timco & Weeks, 2010; Weiss & Marsan, 2004) and waves (Dumont et al., 2011; Horvat & Tziperman, 2015; Kohout & Meylan, 2008; Ren et al., 2021; Williams et al., 2013), as well as the complex dependency of fracturing on the heterogeneous nature of sea ice (Han et al., 2024; Timco & Weeks, 2010).

Parameterized models of floe size and thickness distributions have been used to represent the effect of floe-scale processes in climate models (Bateson et al., 2020, 2022; Boutin et al., 2020; Roach et al., 2018, 2019; Williams et al., 2013). Discrete element models (DEMs), with explicit representations of floes, can also help elucidate the dynamics of floe-scale processes and may provide a path toward developing more advanced parameterizations (Brenner et al., 2023; Herman, 2013; West et al., 2022). DEMs have been effectively used to study the influence of waves on sea ice breakage (Herman, 2017; Montiel & Squire, 2017) and the effects of winds in setting the floe size and thickness distribution within narrow straits (Manucharyan & Montemuro, 2022; West et al., 2022). An idealized DEM coupled to a realistic model of the ocean showed that surface eddies can govern both the motion and melt rate of individual floes (Gupta et al., 2024; Gupta & Thompson, 2022), and enhance lateral melt enough to affect the largest floe sizes (1–50 km) (Horvat et al., 2016).

This work explores the spring-to-summer transition of sea ice over Baffin Bay, a region west of Greenland characterized by easily distinguishable floes during those months. We use the LS-ICE DEM and the satellite imagery introduced in Moncada et al. (2023) to diagnose the relative contributions of breakage and melt in governing the evolution of sea ice concentration and FSD between June and July 2018. We focus on the summer season because satellite imagery is more readily available to help calibrate the model and because the relevant floe-scale processes are simpler to represent than in the winter. Although Baffin Bay provides an observationally constrained target for our base simulation, the primary goal of this study is to assess the sensitivity of the spring-to-summer sea ice mass loss to model parameters across a suite of simulations that may represent a range of different environmental conditions.

Given our focus on process analysis, we introduce a number of simplifications that allow us to conduct a large number of sensitivity simulations while keeping the parameter space and computational expense tractable. We only resolve floes that have an effective diameter greater than 2 km (a threshold set by the satellite image resolution) while representing all other ice via a thickness distribution. Sea ice is thermodynamically coupled to a slab ocean, which redistributes surface heat laterally via a turbulent ocean diffusivity, but does not simulate ocean currents. Floe fracture is achieved via a prescribed and constant breakage rate applied over all resolved floes. Despite these simplifications, the model can reproduce the evolution of domain-averaged sea ice and surface ocean metrics during the period of interest, as inferred from satellite imagery and ocean re-analysis.

Our analysis quantifies the temporal evolution of the FSD and the relative importance of melt and breakage on FSD changes for floes with diameters ranging between 2 and 50 km. In the parameter regime that best fits observations, breakage and melt play comparably important roles in governing the summertime sea ice decline, with breakage being particularly important for the decay of floes larger than 21 km. Future work with more complex breakage schemes (Dumont et al., 2011; Horvat & Tziperman, 2015; Kohout & Meylan, 2008; Williams et al., 2013) and two-way coupling with a dynamic ocean (Gupta & Thompson, 2022) will help further refine and parse the role of individual processes encapsulated within the bulk breakage and melt parameters considered here. Processes shaping floe-scale evolution of sea ice are complex. This study offers a simple framework for understanding the relative importance and scale-dependence of these mechanisms.

The paper is structured as follows: Section 2 describes the model used to represent sea ice melt and breakage processes, the observational data sources, the selection of best fit parameters to observations and the metrics to quantify sea ice changes. Section 3 presents results pertaining to sea ice loss rate and floe size evolution and their sensitivity to key model parameters. Section 4 discusses our results and Section 5 provides closing remarks.

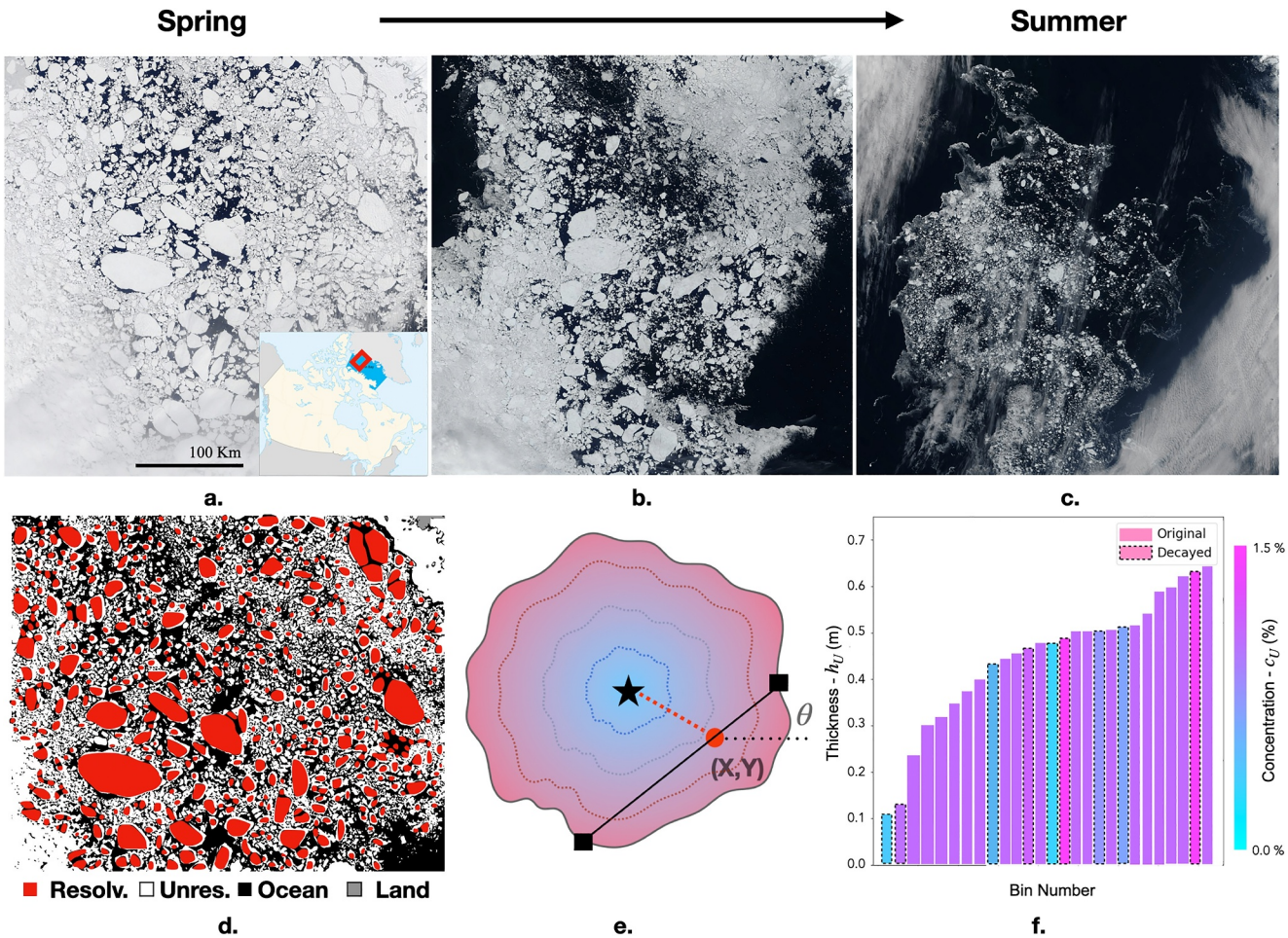

Figure 1. (a–c) Snapshots of NASA MODIS imagery taken within Baffin Bay on (a) 6 June 2018, (b) 28 June 2018, and (c) 24 July 2018, illustrating rapid loss of sea ice during the melt season (from > 60% concentration to almost ice-free) for the region 78.1°W to 61.2°W and 67.9°N to 80.1°N. The inset in the lower right of panel (a) indicates the location of this domain. (d) Characteristic segmentation of the image into resolved floes (red) and unresolved floes (white), with ocean (black) and land (gray). (e) Level-set representation of resolved floes by the LS-ICE model. Each resolved floe carries its own thickness distribution grid. Breakage of resolved floes is idealized as a straight line with random orientation (θ) and random location (X,Y). (f) Schematic illustrating the bins of unresolved floes ordered by increasing thickness h_U. The unresolved sea ice concentration of each bin is indicated by the color scheme and sums to c_U. The bars corresponding to original unresolved floes have no border, whereas those corresponding to "decayed" floes have a dashed border.

2. Methods

2.1. The LS-ICE Model

This work makes use of the level set discrete element model for sea ice (LS-ICE), introduced in Moncada et al. (2023), to study the evolution of sea ice during the spring-to-summer transition of marginal ice zones. The reference simulation is calibrated to reproduce the evolution of sea ice concentration within Baffin Bay (see Figure 1). The domain size is 400 km × 400 km with periodic boundary conditions, such that we do not simulate net lateral heat flux or sea ice advection into the system. Here, LS-ICE represents the idealized physics of individual sea ice floes interacting with a thermodynamic slab ocean, with prescribed solar radiation.

LS-ICE uses level set functions to define the geometry of arbitrarily shaped (non-convex) floes (Harmon et al., 2020; Kawamoto et al., 2016, 2018). "Resolved" floes, defined as pieces of ice with a characteristic diameter greater than 2 km, are represented explicitly by LS-ICE and are the main focus of our study. "Unresolved" floes, whose diameter is smaller than 2 km, are not explicitly modeled by LS-ICE, but are represented statistically (see Figure 1f and description below). During a fracture event, a resolved floe is split into two smaller ones using a straight line, whose orientation and location within the broken floe perimeter are chosen randomly. Fracturing occurs at a prescribed and constant breakage rate B, which represents the number of breakage events

occurring per unit time over the entire floe population. The parameter B may represent the combined effect of various fracture processes such as breakage induced by waves, floe collisions and oceanic or wind drag forces. We acknowledge that this constant fracture rate and the random floe splitting do not reflect the complexity of sea ice fracture mechanisms and their episodic nature, but here, combined with the melt processes, they produce a reasonable evolution of sea ice concentration and FSD slope inferred from satellite imagery for floes larger than 2 km at approximately weekly time scales.

Each resolved floe carries a 2-D sea ice thickness grid in the horizontal direction. The resolution of the local "Lagrangian" grids vary slightly with floe size and geometry, with a characteristic mesh size ranging from 500 m × 500 m to 1 km × 1 km. Additionally, a global "Eulerian" grid carries a surface ocean temperature field, is square, and has a resolution of 1 km. The local and global grids communicate with each other via the thermodynamic equations detailed in Section 2.2. For simplicity, we do not consider cells that are only partially covered by resolved sea ice floes. Instead, at each time step, a level set detection algorithm is used to determine whether the center of a given global grid cell is covered by a resolved floe. If true, the whole cell is considered covered by a resolved floe, but if false, the cell is considered entirely free from resolved floes. For sensitivity, we conducted an experiment with a more sophisticated grid detection algorithm that accounts for partially covered grid cells, but that method was significantly more computationally expensive and did not yield noticeably different results, so we choose the simpler method instead.

Unresolved floes are assumed to be spread uniformly over the global grid cells that are not considered covered with resolved floes. We subsequently refer to global "resolved grid cells" or "unresolved grid cells" depending on whether they contain resolved or unresolved floes, respectively. The unresolved sea ice is captured by a joint concentration-thickness distribution (Figure 1f) that evolves due to a thermodynamic sink caused by basal sea ice melt (see Section 2.2), and dynamicals source representing input from breakage and "lateral" melt of resolved floes. The initial concentration of unresolved floes is represented by 100 bins of equal sea ice concentration and a thickness h_U sampled from a Gaussian distribution with 0.5 m mean and 0.1 m standard deviation. When a resolved floe becomes smaller than the resolution threshold, its corresponding concentration is added to the unresolved distribution as a new bin with a thickness corresponding to the average thickness over the previously resolved floe. The sea ice concentration of each bin is assumed to remain constant over time, as we do not represent lateral melt or breakage for unresolved floes. The unresolved floe concentration can thus only reduce when bins reach zero thickness and are removed from the distribution.

2.2. Thermodynamics

The 2-D local thickness fields of all resolved floes are initialized as uniform. Localized melt occurs in response to heat exchanges with a slab ocean and prescribed atmospheric heat fluxes, with the thickness field evolution described by Moncada et al. (2023):

$$\rho_i L_f \frac{\partial h}{\partial t} = q_v (T_{melt} - T) - S(1 - a_i) + (A_o + B_o T_{melt}), \tag{1}$$

where $h = h(x, y, t)$ is the resolved floe thickness, $T = T(x, y, t)$ is the ocean temperature under the ice, q_v is the ice/ocean heat exchange parameter and S is the solar heat flux. Other constants are specified in Table 1 and in Moncada et al. (2023). There is no explicit parameterization of lateral melt, but the model keeps track of the thickness distribution across the floe, whose evolution is determined by the local basal heat flux. The resolved thickness grid typically allows floes to melt faster at their edges, where ocean temperatures tend to be higher. An effective lateral melt may thus be inferred from the spatial distribution of vertical melt. This representation of lateral melt is likely appropriate for the large floes considered here, whose basal area is considerably larger than the peripheral area (see Section 3.5). Floe formation through sea ice growth is not represented in our simulations and is unlikely to be important during summer in the MIZ.

The ocean temperature below resolved floes evolves according to:

$$\rho_0 c_p H \frac{\partial T}{\partial t} = \rho_0 c_p H k \nabla^2 T - q_v (T - T_{melt}), \tag{2}$$

Table 1
Model Parameters Used in the LS-ICE Simulations

Variable	Meaning	Value	Units
ρ_o	Ocean density	1,030	kg m^{-3}
c_p	Ocean-specific heat capacity	3,991	J kg^{-1} °C^{-1}
H	Mixed layer depth	25	m
k	Ocean horizontal diffusivity	100	m^2 s^{-1}
a_i	Ice albedo	0.7	None
a_o	Ocean albedo	0.3	None
A_o	Atmospheric heat flux linear term	36.6	W m^{-2}
B_o	Atmospheric heat flux linear term (slope)	4.8	W m^{-2} °C^{-1}
T_{melt}	Fusion temperature of sea ice	−1.8	°C
n_{cells}	Total number of cells in domain	160,000	None
A_{cell}	Area of global temperature grid cell	1	km^2
A_T	Total area of domain	160,000	km^2
ρ_i	Ice density	910	kg m^{-3}
L_f	Latent fusion heat of ice	330,000	J kg^{-1}
N_f	Number of resolved floes	493	None
B	Breakage rate	57.6	d^{-1}
q_v	Ice/ocean heat exchange	100	W m^{-2} °C^{-1}
S	Solar flux	240	W m^{-2}

Note. All parameters are kept constant except for q_v, B and S. The values shown here for these latter parameters correspond to the best fit simulation. The number of floes N_f reported here is the value at the initial time step.

where H is the uniform mixed layer depth and k is a prescribed horizontal diffusivity. Sea ice is assumed to be entirely insulating to solar heat fluxes, such that there are no atmospheric heat flux terms in Equation 2. Basal melt produces localized patches of cold temperatures underneath resolved floes, as oceanic heat is delivered to the ice. For simplicity, we do not consider changes in salinity and the associated changes of the mixed layer depth due to sea ice melt. The constant mixed layer depth chosen in this study is meant to average over these spatial and temporal variations.

All floes are advected using the same velocity taken as the observed mean sea ice drift velocity within the region of interest, as estimated from the NSIDC Polar Pathfinder data set at daily resolution (see Section 2.3). Motions occurring at finer temporal scales, such as those induced by inertial oscillations or sub-mesoscale ocean variability, may also be important but are not considered in this work. Sea ice motion allows floes to access warmer waters located around the cold patches produced by resolved floes, and therefore accelerates their melt rate (Gupta & Thompson, 2022).

Unresolved floes (less than 2 km in diameter) are represented as a distribution of sea ice area over characteristic thickness bins, which is initially assumed to be Gaussian (see Figure 1f). These unresolved floes do not exchange momentum with the resolved floes and are assumed to be uniformly distributed over all global grid cells that are not occupied by the resolved floes. The net albedo and outgoing longwave radiation temperature for these grid cells is thus computed based on a mixture between open ocean and unresolved ice concentration (see details in Moncada et al. (2023)). The thickness of a given unresolved floe bin decreases due to melt from ocean and atmosphere heating, whereas its concentration remains constant. The unresolved floe thickness (h_U) evolves using the following equation:

$$\rho_i L_f \frac{\partial h_U}{\partial t} = q_v\left(T_{melt} - \tilde{T}_f\right) - S(1 - a_i) + (A_o + B_o T_{melt}), \quad (3)$$

where $\tilde{T}_f$ is the average ocean temperature over unresolved cells. After a bin thickness reaches zero, the corresponding sea ice area (or concentration) disappears. When resolved floes break into pieces that are too small to track, their concentration and thickness are added to the unresolved floes distribution, such that the total sea ice mass is conserved during fracturing. The ocean temperature underneath cells that do not contain a resolved floe evolves as follows:

$$\rho_0 c_p H \frac{\partial T}{\partial t} = \rho_0 c_p H k \nabla^2 T - q_v c_U \left(\tilde{T}_f - T_{melt}\right) + S(1 - c_U)(1 - a_o) - (1 - c_U)(A_o + B_o T), \quad (4)$$

where c_U represents the unresolved sea ice concentration.

2.3. Observational Data Products

This work makes use of observational products to help constrain the parameters of the LS-ICE model in the baseline simulation (see Table 1). We choose to focus on a 400 km × 400 km region within Baffin Bay (approximate coordinates between 78.1°W and 61.2°W, and 67.2°N and 80.1°N) between June 6 and July 24 of 2018, as shown in Figure 1a. We collect a sequence of daily satellite images from the NASA MODIS optical data set at 500 m resolution (MODIS Science Team, 2017). We manually discard the images that are too cloudy or those with a segmentation negatively impacted by relatively sparse cloud cover, which leaves a total of 18 images used for the analysis out of the 48 possible snapshots (see Figure 5b). During the period considered, sea ice evolves from a relatively loose mosaic composed of individual floes to an almost completely ice-free ocean.

We identify floes by first detecting ice versus ocean pixels using a brightness threshold varying between 190 and 200 (from the range of 0–255), and subsequently segmenting individual floes using a watershed algorithm (Lopez-Acosta et al., 2019; Moncada et al., 2023). Given the image resolution, we can only reliably detect floes with size greater than approximately 2 km of equivalent diameter. The identified floes are used to initialize the resolved floe shapes in the DEM at the start of the simulations (on 6 June 2018) and for subsequently tracking their concentration and size distribution evolution. Pixels classified as sea ice that are not identifiable as individual floes are labeled as part of the unresolved floe concentration.

We additionally leverage re-analysis products of the atmosphere, ocean, and sea ice to further help constrain parameters of the LS-ICE model. For the atmospheric heat fluxes, we use the ERA5 Global Atmospheric Reanalysis data set (Hersbach et al., 2023), with a spatial resolution ranging from 0.25° × 0.25° to 1° × 1° and hourly temporal resolution. Sea ice velocities are obtained from the National Snow and Ice Data Center (NSIDC) Polar Pathfinder Sea Ice Motion Vectors (Tschudi et al., 2019), which has a daily temporal resolution and a 25 km × 25 km spatial resolution. For the ocean, we use the Arctic Ocean Physics Reanalysis product stored within the Copernicus Database (European Union-Copernicus Marine Service, 2024). This reanalysis product has 12.5 km × 12.5 km spatial resolution and a daily temporal resolution. From this data set, we obtain sea ice thickness, ocean mixed layer depth, and the surface value of sea water potential temperature. Given the sparseness of in situ ocean data in polar regions, particularly under ice, we note that there may be significant uncertainties associated with these data products.

2.4. Model Fitting Procedure

The observational products over Baffin Bay are used to callibrate a baseline simulation within LS-ICE. Our goal is to broadly capture the statistical evolution of sea ice and the upper-ocean, rather than to reproduce the exact behavior of individual floes. We choose the region within Baffin Bay highlighted in Figure 1a, because we can visually identify several of the same large floes staying within the region of interest throughout the period considered (June 6–July 24, 2018). According to the Arctic Ocean reanalysis data set described in Section 2.3, the sea ice drift speeds averaged over this region range from 0.1 to 5.1 km/day (mean 1.7 km/day). Given that our domain size is 400 km × 400 km, a significant fraction of sea ice is estimated to remain within the region over the course of the period of interest (48 days). However, further work would be required to more precisely quantify the effect of net lateral advection of both sea ice and heat into the domain. At the start of the simulation period (June 6) the conditions are: 18% resolved floe concentration, 44% unresolved sea ice concentration, −1.5°C initial mean surface ocean temperature, and 0.5 m initial average ice thickness.

The fitting procedure is designed to constrain the values of the following parameters: ice/ocean heat exchange parameter q_v and breakage rate B. The rest of the parameters are fixed to the values summarized in Table 1. For simplicity and ease of conducting the sensitivity analysis, we choose all model parameters to be temporally invariant, representing a characteristic value over the time frame of interest (Table 1). The solar flux S is set to the nonclear sky value obtained from ERA5. The outgoing energy flux parameters A_o and B_o are obtained by considering the sum of the net outgoing longwave flux, sensible heat flux, and latent heat flux in ERA5. This total outgoing flux is found to be well represented by a linear fit to the surface temperature. Finally, the mixed layer depth H is taken as the time average value from the Arctic Ocean Physics reanalysis. We confirm that for this set of parameters, the following energy budget of the combined ice-ocean system is well balanced:

$$\rho_0 c_p H \frac{\Delta \bar{T}}{\Delta t} + \rho_i L_f \frac{\Delta h}{\Delta t} \approx S(1 - \bar{a}) - \left(A_o + B_o \bar{T}\right), \tag{5}$$

where $\Delta \bar{T}$ is the change in mean ocean temperature, Δt is the duration of the simulation, Δh is the change in average ice thickness, and $\bar{a}$ is the average albedo.

The breakage rate B and ice/ocean heat exchange parameter q_v are subsequently fit by conducting sensitivity simulations over a range of these parameters, and minimizing the error in the resolved and unresolved floe concentrations, and in the FSD evolution (see Section 3 and Supporting Information S1). The error in resolved floe concentration is strongly sensitive to B, which helps to constrain its value to approximately $B = 40$–$70\ \mathrm{d}^{-1}$ (Figure S2 in Supporting Information S1).

The evolution of the unresolved floe concentration is highly sensitive to q_v, but less sensitive to B. The unresolved error is minimized for $q_v = 30$–$105\ \mathrm{W\ m^{-2}{}^{\circ}C^{-1}}$ (Figure S2 in Supporting Information S1). Taking into consideration the total concentration error and the FSD slope error helps further constrain the remaining model parameters to $q_v = 100\ \mathrm{W\ m^{-2}\ {}^{\circ}C^{-1}}$ and $B = 57.6\ \mathrm{d}^{-1}$ (Figure S2 in Supporting Information S1). Finally, we find that resolved floes are not very sensitive to the ocean diffusivity k in the range 1–$400\ \mathrm{m^2\ s^{-1}}$. We therefore fix k to a reasonable value of $100\ \mathrm{m^2\ s^{-1}}$ representing sub-mesoscale mixing in the presence of sea ice floes with an average radius of about 5 km (Gupta & Thompson, 2022).

Because of the model idealizations and relatively sparse observations, it is not possible to find a set of parameters that minimizes the error for all observed quantities. Here, we choose to prioritize capturing the evolution of the resolved and unresolved floe concentration with respect to B and q_v, respectively, as well as choosing a q_v value that is within the range of observations (McPhee, 1992). Future work using more realistic representations of unresolved floes and a dynamic evolution of the mixed layer depth, would help further assess the impact of our approximations on the behavior of the coupled system.

2.5. Model Diagnostics

2.5.1. Sea Ice Mass Loss Rate

The main diagnostic we use to track changes in sea ice is the mass loss rate of resolved floes. Although concentration changes are a useful metric for tuning the model, we focus our analysis on mass, as it allows a decomposition of the sea ice loss into breakage, solar, oceanic, vertical, and lateral melt contributions. The total resolved floe mass at a given time step is calculated as follows:

$$m_R = \rho_i \Sigma_{k=1}^{N_f} \Sigma_{j=1}^{N_c} A_k^j h_k^j, \tag{6}$$

where N_f is the total number of floes, N_c is the total number of cells in a particular sub-floe grid, j is the index of a sub-floe grid cell belonging to a floe k, and A and h are the respective area and thickness of each cell. The net mass loss rate averaged over the entire simulation is then estimated as follows:

$$\bar{m}_R = \frac{dm_R}{dt} = \frac{m_R^{\mathrm{f}} - m_R^0}{\Delta t_{loss}}, \tag{7}$$

where m_R^0 and m_R^f are the masses of resolved floes at the start and end of the simulation, respectively, and Δt_{loss} is the time taken for the resolved floes to completely disappear from the domain. If some resolved floes remain at the end of the simulation, Δt_{loss} is taken as the total simulation time. Our simulations assume no refreezing, hence the total sea ice mass and concentration always decline with time, and we report the rates in absolute values for convenience.

2.5.2. Floe Size Distribution Slope

We evaluate the floe size distribution (FSD) at a given time step as the number distribution of floes within the domain binned over characteristic sizes (Leppäranta, 2011). We define the size of a floe with arbitrary shape as the diameter of an equivalent disk with the same area as the original floe (Hwang et al., 2017; Montiel & Squire, 2017). We then characterize the floe size distribution using the cumulative floe number distribution (CFND) binned over their equivalent diameter. We estimate the slope of the CNFD β by performing a linear regression in log-log space for all points of the FSD. When the largest floes or any bin disappear from the domain due to breakage and melt, we remove these bins, such that the zeroes of the CFND are not included in the calculation of β. Following Hwang et al. (2017), we estimate the FSD exponent from the cumulative distribution exponent as:

$$\alpha = |\beta| - 1. \tag{8}$$

A higher value of α implies a bigger fraction of small floes relative to larger floes. We note that there are more accurate methods for estimating the FSD, obtaining the power coefficient α and quantifying the goodness of the power law fit, such as the maximum likelihood estimate (MLE) and others (Clauset et al., 2009; Stern, Schweiger, Stark, et al., 2018). However, we find that the MLE does not provide reliable estimates of the FSD here, due to the relatively narrow range of scales (2–50 km) modeled by our method and the limited total number of floes considered. We therefore choose the direct power-law method as a metric to characterize the FSD evolution across different breakage and melt parameters, but acknowledge that it may not be a comprehensive descriptor of floe sizes. We quantify uncertainty in our estimate of the modeled FSD evolution via the variability over an ensemble of simulations with random breakage events.

3. Results

3.1. Phenomenology

Figure 2 shows snapshots of the observed sea ice floes considered "resolved" by the floe detection algorithm (see Section 2.1), alongside corresponding snapshots from selected simulations. Both the model and observations illustrate the progressive decline in resolved sea ice concentration. In the observations and the best-fit simulation ($B = 58$ d^{-1}), the resolved and unresolved floe concentrations reduce with each subsequent snapshot. In a sensitivity simulation with higher breakage rate ($B = 86$ d^{-1}), this reduction also occurs, but at a slightly accelerated rate. In a simulation with low breakage rate ($B = 2$ d^{-1}), the smaller floes disappear from the domain, but the large floes tend to remain, such that the resolved floe concentration does not decline as rapidly. In the following sections, we explore the balance between breakage and melt processes in controlling the evolution of the resolved floes.

The resolved sea ice floes have a clear signature on localized ocean temperature due to the albedo and insulating properties of sea ice (Figure 3). Larger floes generate persistent cold ocean patches, which partially shield them from lateral heat fluxes that originate from the prescribed ocean diffusivity and floe motions. The increase in total resolved floe perimeter due to breakage may also help increase lateral melt. However, this effect is likely limited in our simulations because all floes have the same velocity, such that the individual pieces originating from a broken floe stay next to each other. On the other hand, the conversion of floes from resolved to unresolved due to breakage clearly allows temperature to increase locally, since unresolved floes are assumed to be uniformly distributed over the grid cells that do not contain resolved floes.

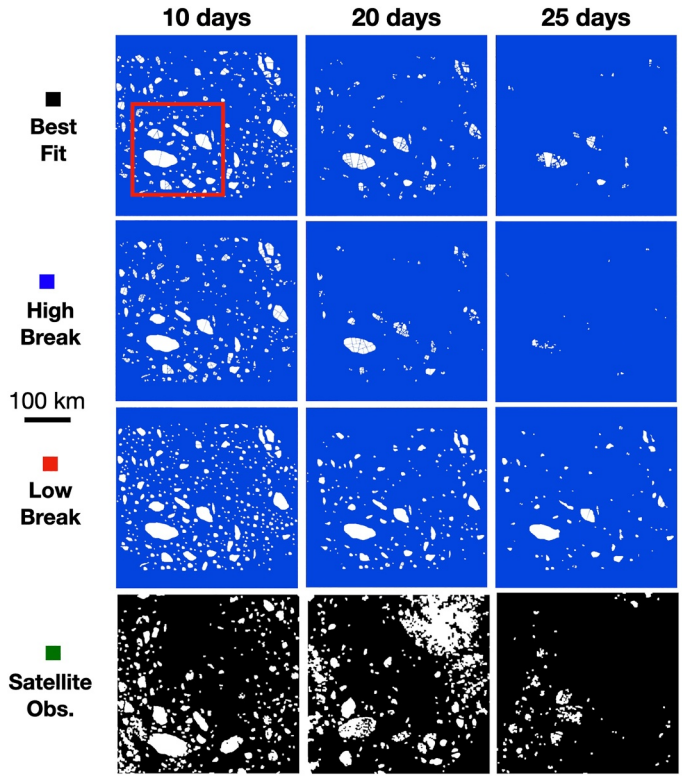

% Conc.	10 days	20 days	25 days
Resolved	14.3	6.4	2.4
Unresolved	47.1	11.5	3.5

% Conc.	10 days	20 days	25 days
Resolved	13.0	4.6	1.5
Unresolved	48.8	10.7	2.0

% Conc.	10 days	20 days	25 days
Resolved	16.7	10.1	5.8
Unresolved	44.1	4.7	1.3

% Conc.	10 days	20 days	25 days
Resolved	12.5	9.4	2.9
Unresolved	41.6	31.4	14.3

Figure 2. Snapshots of resolved floes in the best fit simulation (top row, $B = 58\ \mathrm{d}^{-1}$), high break simulation (second row from top, $B = 86\ \mathrm{d}^{-1}$), low break simulation (third row from top, $B = 2\ \mathrm{d}^{-1}$) and processed satellite images (bottom row). Each row also includes a table that displays the resolved and unresolved sea ice concentration at the different time stamps. The corresponding α evolutions are shown in Figure 5. The red frame in the upper left snapshot shows the area considered in Figure 3.

3.2. Contributions to the Mass Loss of Resolved Floes

In our simulations, resolved floes are lost due to a combination of solar and oceanic melt, as well as breakage into unresolved floes. The relative importance of these mechanisms in driving the average mass loss of resolved floes $\bar{m}_R$ can be examined by considering the following decomposition:

$$\bar{m}_R = \bar{m}_B + \bar{m}_S + \bar{m}_O, \tag{9}$$

where $\bar{m}_B$, $\bar{m}_S$, $\bar{m}_O$ are the average mass loss rates of resolved floes due to breakage, solar melt and oceanic melt, respectively. Floes are considered lost due to breakage when they fracture into pieces that are smaller than the resolution threshold at 2 km. The solar and oceanic components are calculated from the relevant terms in Equation 1.

The simulation with the best fit to observations exhibits the following split: $\bar{m}_B : \bar{m}_S : \bar{m}_O = 0.32{:}0.47{:}0.21$, such that solar melt dominates, followed by breakage and oceanic melt. We investigate the sensitivity of the resolved floe mass loss rate and the split between each of its contributions in Equation 9 by conducting a suite of simulations varying the breakage rate B, the ice/ocean heat exchange parameter q_v and the solar constant S (Figure 4). The resulting scenarios represent different environmental regimes that may occur over the course of a given melt season, in different regions, or as part of inter-annual variability.

The sensitivity of sea ice mass loss to breakage and melt is investigated by varying B and S for a fixed q_v at the best fit value. Increasing S directly accelerates surface melt and can indirectly enhance basal and lateral melt by warming the surrounding ocean. Increasing B accelerates the mass loss of resolved floes by reducing the size of floes beyond the resolution threshold and by promoting lateral melt via an increase in the total perimeter of

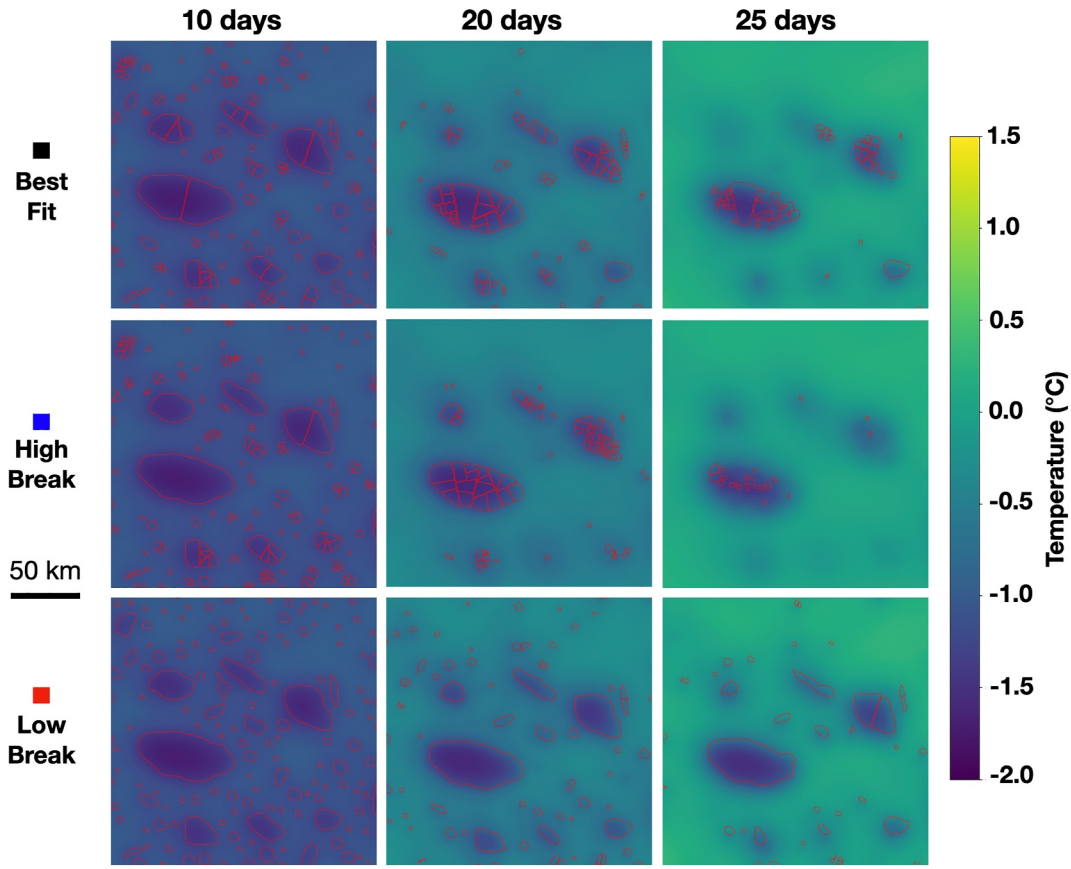

Figure 3. Snapshots of ocean temperature for the area highlighted in Figure 2, and for the same conditions as in Figures 2 and 5. The outlines of resolved floes are marked in red.

resolved floes. In the vicinity of the best fit simulation parameters, B and S both influence the loss of floes, but under the high breakage regimes (large B), B plays a more dominant role (Figure 4a).

The relative importance of breakage versus melt can be quantified via the following ratio:

$$\mu_{BM} = \frac{\bar{m}_B}{\bar{m}_S + \bar{m}_O}. \tag{10}$$

For the best fit simulation, $\mu_{BM} = 0.47$, such that melt dominates over breakage-induced loss. This result is consistent with the characteristic time scales associated with breakage and melt, respectively (Section 4 in SI). Figure 4c shows that μ_{BM} is strongly controlled by B and varies between a melt-dominated regime ($\mu_{BM} < 1$ at low B) and a breakage-dominated regime ($\mu_{BM} > 1$ at higher B).

We next investigate interactions between solar and oceanic melt by varying q_v and S for B fixed at the best fit value. The loss of resolved floes is equally sensitive to changes in q_v and S for the entire parameter space explored here (Figure 4b). This suggests that solar and oceanic melt do not strongly compete against each other, but that they independently promote a greater mass loss of resolved floes.

The relative contribution of oceanic and solar melt is quantified via the following ratio:

$$\mu_{OS} = \frac{\bar{m}_O}{\bar{m}_S}. \tag{11}$$

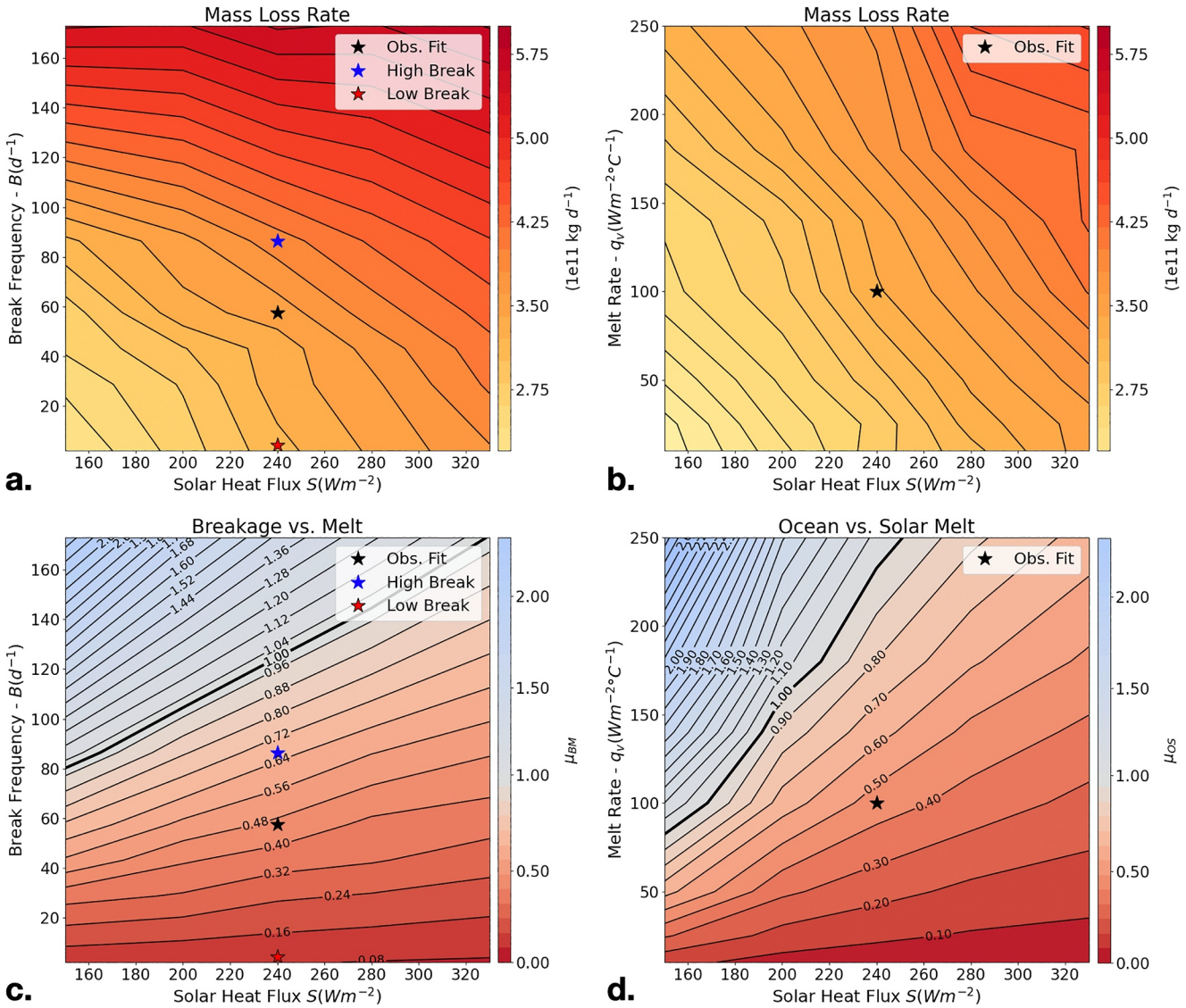

Figure 4. (a) Sensitivity of the mass loss rate of resolved floes to the solar heat flux S and the breakage frequency B. A total of 42 simulations were run with B linearly varying from 2 to 173 d^{-1} and S varying from 150 to 330 Wm^{-2} (b) Same as in (a), but for varying q_v and S. A total of 36 simulations were conducted, linearly varying q_v between 5 and 250 Wm^{-2} °C^{-1} and S between 150 and 330 Wm^{-2} (c) Ratio of breakage to melt contribution μ_{BM} (Equation 10) evaluated from the same simulations as in (a). (d) Ratio of oceanic to solar melt contribution μ_{OS} (Equation 11) evaluated from the same simulations as in (b). The stars indicate the best-fit simulation (black), a high-breakage scenario (blue), and a low-breakage scenario (red).

For the best fit simulation, $\mu_{OS} = 0.46$, such that solar melt dominates over oceanic melt. The parameter μ_{OS} is strongly sensitive to S for lower S and higher q_v values. For lower S and lower q_v values, the sensitivity of μ_{OS} to q_v increases. In the regime close to the best fit scenario, μ_{OS} is equally sensitive to q_v and S. (Figure 4d).

3.3. FSD Evolution and Sensitivity to Breakage Rate

The importance of breakage for the loss of large sea ice floes and its interactions with melt can be further investigated by examining the evolution of the FSD throughout the simulation time period. In the best-fit scenario, the FSD slope α, calculated from Equation 8, increases with time as the proportion of large floes diminishes relative to the smaller floes (Figure 5a).

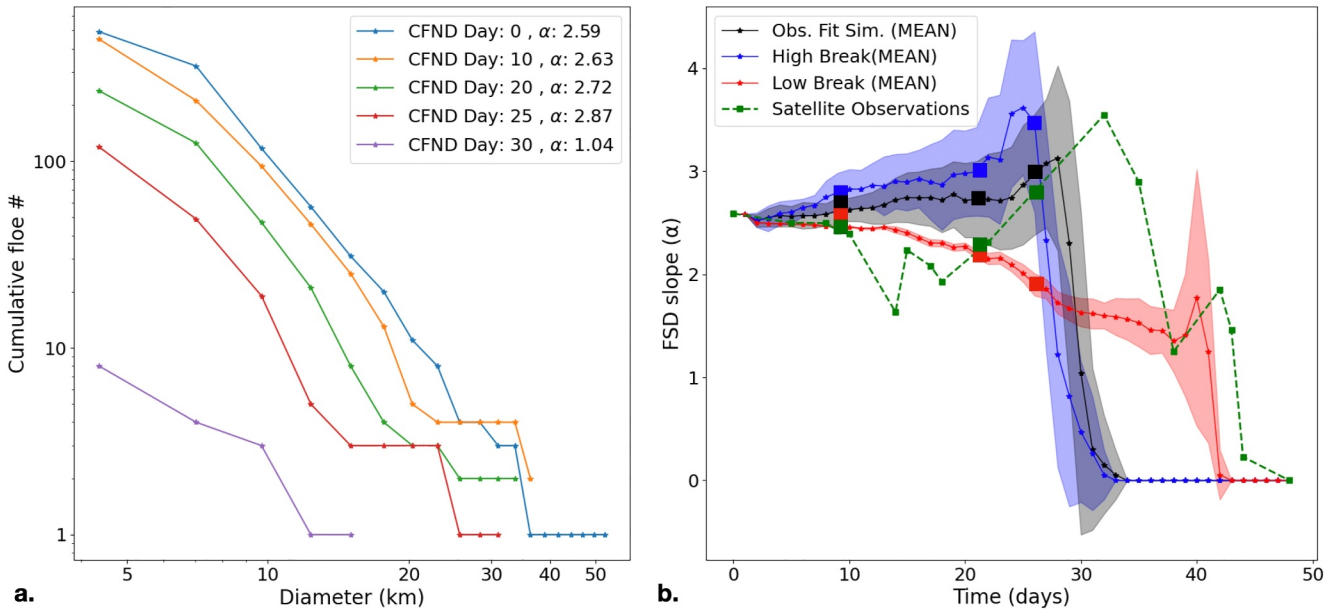

Figure 5. (a) Cumulative Floe Number Distribution (CFND) at various time steps for one of the simulations belonging to the best-fit ensemble. The corresponding FSD coefficient α is indicated in the legend. (b) Time-evolution of α for the best fit (black, $B = 58\ \mathrm{d}^{-1}$), high break (blue, $B = 86\ \mathrm{d}^{-1}$), and low break (red, $B = 2\ \mathrm{d}^{-1}$) simulation scenarios, along with observations (green). The shading represents the standard deviation spread calculated for 20 ensemble members of each scenario. The small green squares represent days where satellite imagery was relatively cloud-free and used for model callibration.

The observed α from satellite imagery snapshots shows a slight decline for the first 20 days of the data collection period, followed by a steep increase between days 20 and 30, and a sharp decline between days 30 and 50, until all resolved floes have disappeared from the domain (Figure 2). The best fit model ensemble ($B = 58\ \mathrm{d}^{-1}$) displays a comparable FSD evolution to observations, with weak changes in the first 20 days, a stronger increase between days 20 and 30, followed by a steep fall before the last days of the simulation (Figure 5b). A "high breakage" scenario ($B = 86\ \mathrm{d}^{-1}$) shows a steady and large increase in α during the first 25 days of the simulation followed by a fast reduction, illustrating the effect of breakage in steepening the FSD profile faster and earlier compared to scenarios with slower breakage. In contrast, a "low breakage" case ($B = 2\ \mathrm{d}^{-1}$) displays a steady decline in α, until melt reduces floe number significantly, which highlights the effect of this melt in shoaling the FSD slope. We also note that a larger initial FSD slope leads to a faster decline of sea ice (Figures S3 and S4 in Supporting Information S1), as it provides a greater surface area for melt at a given concentration.

3.4. FSD Tendency Decomposition

Decomposing the flux of ice floes between spatial scales into melt and breakage components provides quantitative insights into the FSD evolution. We can express the FSD tendency as:

$$\frac{df(D)}{dt} = \dot{M}_G(D) - \dot{M}_L(D) + \dot{B}_G(D) - \dot{B}_L(D), \tag{12}$$

where the terms on the RHS represents the tendencies due to melt gain ($\dot{M}_G(D)$), melt loss ($\dot{M}_L(D)$), breakage gain ($\dot{B}_G(D)$) and breakage loss ($\dot{B}_L(D)$), expressed in the number of floes changed in a given equivalent diameter (or bin) D per unit time. Melt gains for a bin with diameter D represent an increase in the number of floes for that specific bin size due to the shrinking of larger floes by lateral melt. Similarly, breakage gains correspond to new floes added to that bin category due to the fracturing of larger floes. Melt and breakage losses indicate floes transitioning into a smaller size due to melt or fracture. The diagnosis of the terms in Equation 12 is carried out at each simulation step and over 20 FSD bins. If floe breakage generates a piece whose size is smaller than the resolution threshold (2 km), the original bin records a breakage loss, whereas the small broken piece is discarded from the resolved FSD and converted to unresolved floe area.

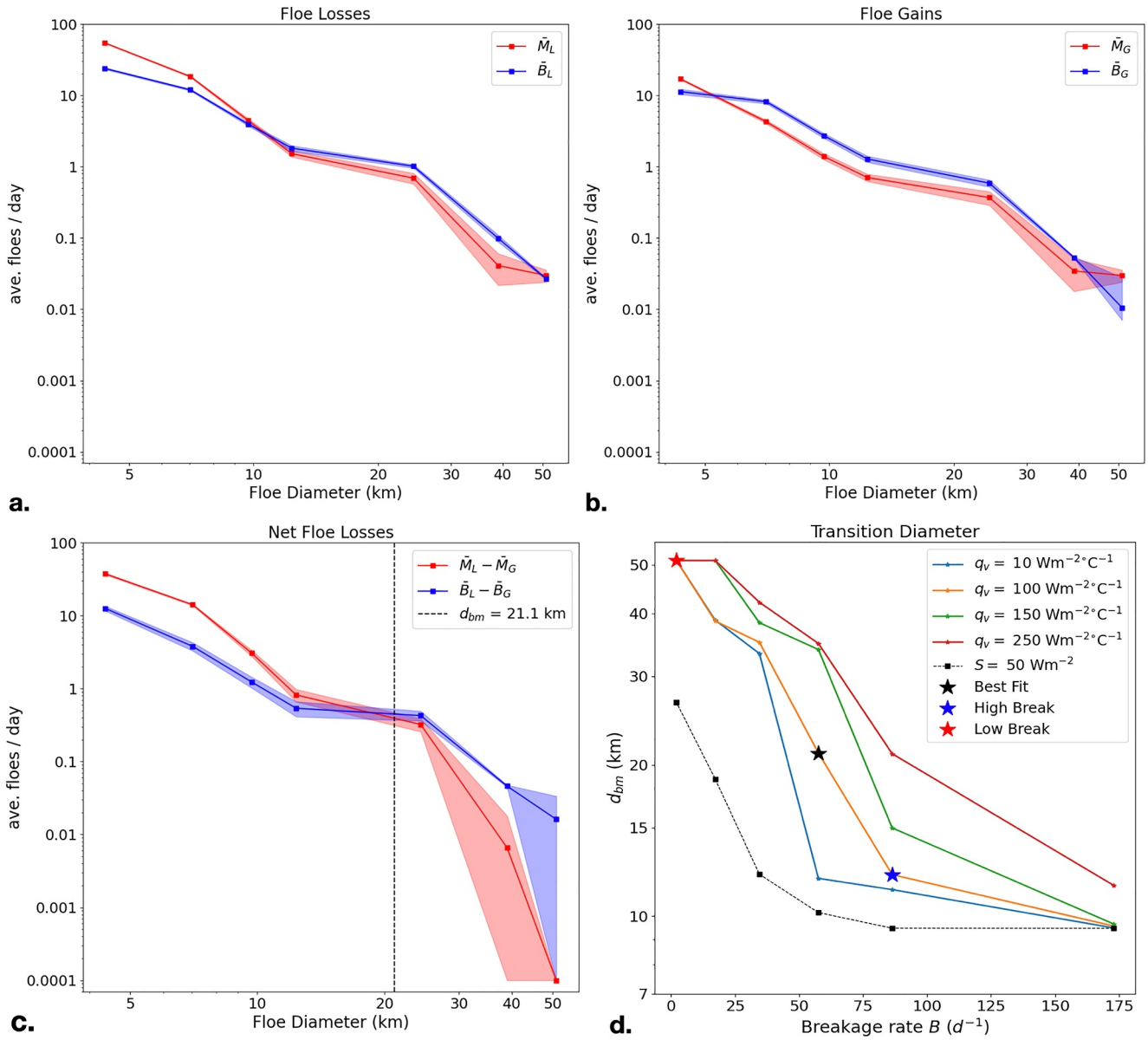

Figure 6. (a–c) FSD tendency decomposition, as expressed in Equation 12, for the simulation ensemble with best fit to observations. Calculations are carried over 7 bins with uneven spacing, ranging between 2 and 50 km, and averaged over days 3–40. The shading indicates one standard deviation variability across the 20 ensemble members. For clarity, terms are clipped to a minimum value of 10^{-4} floes/day. (a) Average loss due to melt $(\bar{M}_L)$ and breakage $(\bar{B}_L)$. (b) Average gain due to melt $(\bar{M}_G)$ and breakage $(\bar{B}_G)$ (c) Average net loss due to melt ($\bar{M}_L$–$\bar{M}_G$) and breakage ($\bar{B}_L$–$\bar{B}_G$). The dashed line indicates the transition diameter d_{bm} separating sizes controlled by breakage for large floes and melt for smaller floes. Note that the location of intersection is slightly distorted in the figure due to log-log plotting. (d) Sensitivity of d_{bm} to B and q_v, with all other parameters kept constant ($S = 240\ Wm^{-2}$). If an S value is provided, then all the other parameters are equal to the values in Table 1. A lower value of d_{bm} indicates a stronger effect of breakage relative to melt in the FSD tendency.

We conduct the FSD tendency decomposition on the best fit scenario, average the terms in Equation 12 over multiple simulations between days 3–40 (Figure 6), and express this average of instantaneous gain or loss rates as $\bar{M}_G(D)$, $\bar{M}_L(D)$, $\bar{B}_G(D)$ and $\bar{B}_L(D)$, respectively. For ease of interpretation, we aggregate the results over 7 characteristic bins. Regarding the floe losses over individual bins, we find that $\bar{B}_L$ is equal to or greater than $\bar{M}_L$ over most bin sizes except for floes smaller than approximately 10 km, where $\bar{M}_L$ dominates (Figure 6a). Similarly regarding floe gains, $\bar{B}_G$ dominates over $\bar{M}_G$ for most bin sizes, except for floes smaller than 5 km or larger than 40 km, where $\bar{M}_G$ plays a stronger role than $\bar{B}_G$ (Figure 6b).

The mean net loss due to breakage $\left(\bar{B}_{net} = \bar{B}_L - \bar{B}_G\right)$ and the net loss due to melt $\left(\bar{M}_{net} = \bar{M}_L - \bar{M}_G\right)$ are shown in Figure 6c. We find that there is a transition diameter $d_{bm} = 21.1$ km (dotted black line in Figure 6c), above which $\bar{B}_{net}$ dominates over $\bar{M}_{net}$, and below which $\bar{M}_{net}$ dominates over $\bar{B}_{net}$. This is consistent with our expectation that the largest floes are less affected by oceanic melt, as their under-ice temperature is often close to freezing.

We next examine the sensitivity of d_{bm} to the breakage rate B and the ice/ocean heat exchange parameter q_v by evaluating the FSD tendency decomposition over a range of sensitivity simulations (Figure 6d). The transition scale d_{bm} tends to decrease as B increases and as q_v decreases, reflecting a larger proportion of net floe losses due to breakage compared to melt. However, for the best-fit value of the solar constant ($S = 240$ W m^{-2}), d_{bm} does not decrease beyond 10 km when increasing B. Moreover, reducing q_v to 10 Wm^{-2}°C^{-1} does not strongly change the values of d_{bm} compared to when q_v is equal to 100 Wm^{-2}°C^{-1}. The presence of these asymptotic limits in d_{bm} is due to the solar forcing, which plays an important role in melting small (2–10 km) floes. Decreasing d_{bm} below the 10 km threshold, and thus further reducing the effect of melt relative to breakage in the FSD evolution, requires a drastic reduction in S and q_v. For example, $S = 50$ Wm^{-2} with $q_v = 100$ Wm^{-2}°C^{-1} still converges to 10 km. A reduction to $S = 50$ Wm^{-2} with $q_v = 0.1$ Wm^{-2}°C^{-1} was found to only produce d_{bm} values down to 8–9 km. Thus, even for this very low values of S and q_v, melt dominates over breakage for floes in the range 2–9 km.

3.5. Lateral Versus Vertical Melt of Resolved Floes

As described in Section 3.2, the melt of resolved floes occurs over individual floe grid cells, based on localized basal and solar heat fluxes. Since the ocean tends to be warmer near the edge of the ice floe, the floe grid cells at these locations can melt faster than over the rest of the floe, leading to lateral shrinking (Figure S5 in Supporting Information S1). The melt of resolved floes may thus be interpreted as a combination of vertical (thickness reduction) and lateral (area reduction) melt, which both contribute to sea ice concentration and mass decline.

We estimate the contributions of lateral versus vertical melt to the FSD tendency explored in Equation 12 and Figure 6. The vertical melt is defined here as the sum of basal and top melt. Over a model time step, a given bin category can reduce its floe count via melt due to floes shrinking (lateral melt), or floes melting out completely (vertical melt). The instantaneous rate of floes lost due to melt $\dot{M}_L$ can thus be decomposed as follows:

$$\dot{M}_L = \dot{M}_L^v + \dot{M}_L^l, \tag{13}$$

where $\dot{M}_L^v$ and $\dot{M}_L^l$ are the vertical and lateral contributions, respectively. We estimate $\dot{M}_L^l$ by assuming that the melt gain at a given bin index $i_D - 1$, is equal to the lateral melt loss contribution from the bin with index i_D, corresponding to larger floes:

$$\dot{M}_L^l(i_D) = \dot{M}_G(i_D - 1). \tag{14}$$

We then obtain the vertical contribution $\left(\dot{M}_L^v\right)$ as a residual from the known total contribution $\dot{M}_L$. We additionally assume that all melt gains of the unresolved floes originate exclusively from lateral losses of the smallest resolved floe bin size.

The lateral melt contribution to the FSD tendency dominates over its vertical melt counterpart for all floe sizes (Figure 7a). For larger floe sizes, the lateral melt contribution diminishes, due to the increase in the ratio between the basal $\left(\bar{A}\right)$ to peripheral $\left(\sim \pi D \bar{h}\right)$ floe area. The vertical contribution to changes in FSD is weak, as it requires the total melt of a floe, which rarely occurs for the large floes considered here.

The lateral melt rate expressed as a reduction of the equivalent floe radius ($D/2$) can be estimated as follows:

$$\dot{\mathcal{L}} = \frac{\Delta D}{2\Delta t}. \tag{15}$$

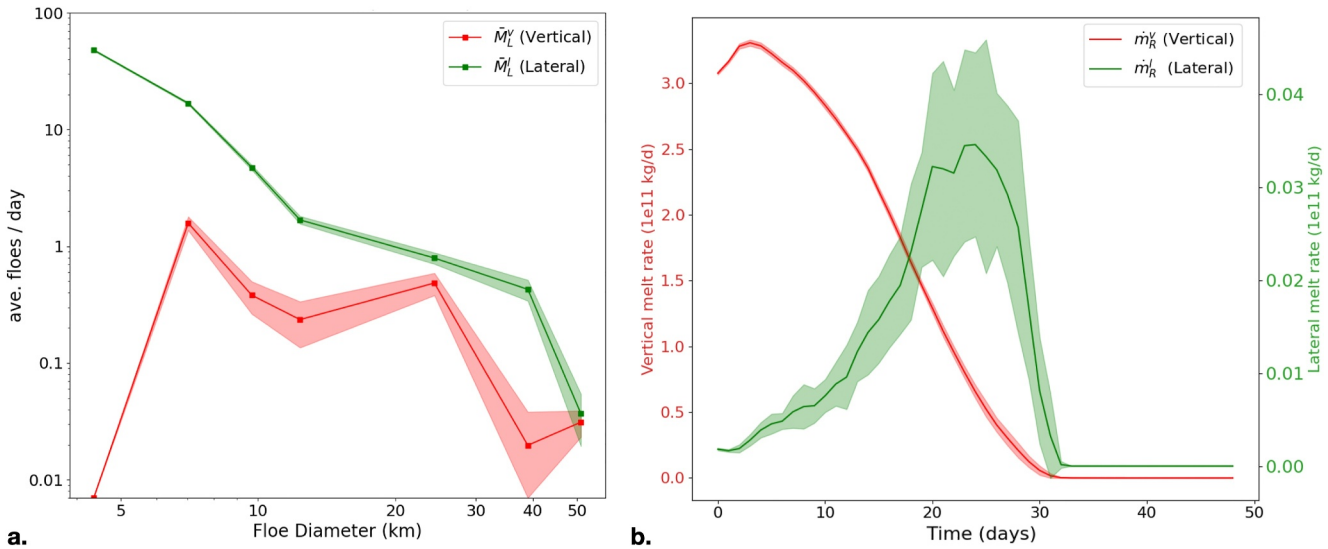

Figure 7. Diagnosed vertical versus lateral melt rates in the best-fit simulation ensemble. The shading represents the standard deviation spread across ensemble members. (a) FSD tendency of floe number loss per day due to average vertical $\left(\bar{M}_L^v\right)$ versus lateral $\left(\bar{M}_L^l\right)$ melt rate decomposed in the same floe size bins as in Figure 6, and calculated following Equations 13 and 14, respectively. (b) Time evolution of the vertical $\left(\dot{m}_R^v\right)$ and lateral $\left(\dot{m}_R^l\right)$ mass melt rates of resolved floes evaluated from Equations 16 and 17, respectively.

When averaged across individual FSD bin sizes, $\dot{\mathcal{L}}$ ranges between 0.1 and 0.6 km/day over the course of the simulation.

We additionally estimate the contributions of vertical $\left(\dot{m}_R^v\right)$ versus lateral $\left(\dot{m}_R^l\right)$ sea ice mass loss for resolved floes as follows:

$$\dot{m}_R^v = \frac{\rho_i}{\Delta t}\Sigma_{k=1}^{N_f}\bar{A}_k\Delta h_k, \tag{16}$$

$$\dot{m}_R^l = \frac{\rho_i}{\Delta t}\Sigma_{k=1}^{N_f}\Delta A_k\bar{h}_k, \tag{17}$$

where k is the floe index, Δt is the time step duration, $\overline{A_k}$ is the average floe area, $\overline{h_k}$ is the average thickness, and ΔA_k and Δh_k are the area and thickness reductions due to melt.

The diagnosed vertical melt rate is approximately two orders of magnitude greater than the lateral melt rate (Figure 7b) for mass changes, largely driven by the large ratio between cross-sectional to peripheral area. For consistency with the lateral melt rate defined in Equation 15, the lateral mass loss in Equation 17 is only registered when the thickness of a given sea ice cell first registers a zero value, which leads to a weak lateral mass loss contribution relative to vertical melt. The vertical mass melt rate declines over time, due the resolved floe mass also declining during the simulation. The lateral mass melt rate tends to increase over time, as floes become smaller due to breakage and have more exposed area, before dropping off sharply when most of the resolved floes have disappeared. We thus note that when considering mass loss, the vertical contribution to melt dominates over the lateral one, since floe diameter is much larger than thickness $\left(Dh < D^2\right)$. On the other hand, when parsing the contribution to FSD trends, lateral melt dominates over vertical melt, as large floes rarely melt out completely from a bin size category.

4. Discussion

The modeling framework employed in this work helps to investigate the spring-to-summer evolution of sea ice at the scale of individual floes. The modeling approach is distinct from past studies using floe-aware sea ice models

(Boutin et al., 2020; Brenner et al., 2023; Gupta et al., 2024; Herman, 2013; Horvat et al., 2019; Manucharyan & Montemuro, 2022; Roach et al., 2018), and offers new insights on interactions between breakage and melt processes. Here, we discuss these results, as well as caveats associated with our modeling framework. These caveats pertain to the difficulty in validating complex processes within the MIZ due to the lack of observations and practical concerns pertaining to the computational expense of LS-ICE and the tractability of the parameter space.

The resolved floes considered in our simulations have an equivalent diameter ranging from 2 to 50 km, which represents the upper-end of observed floe sizes. This focus on large floes complements past studies, which investigated detailed summertime interactions between ocean (sub)-mesoscale turbulence and individual floes that have sizes within this range (Brenner et al., 2023; Gupta & Thompson, 2022; Gupta et al., 2024; Horvat et al., 2016). The key distinction here is a more sophisticated sea ice model, where floes can break and have arbitrary shapes constrained by observations. We find that in the simulation that best fits the observations, breakage plays a first-order role in governing the reduction in resolved floe count, as well as the decline in total sea ice concentration. This result is consistent with past work that considered a statistical rather than resolved representation of sea ice floes (Roach et al., 2018), though some of the mechanisms differ, as discussed below.

Despite the key role played by breakage, our representation of fractures is highly idealized. The breakage rate of sea ice floes is prescribed, occurs at a constant rate, and across random orientations with a given floe. This scheme can capture the initial increase in FSD slope followed by its sharp decline, but the timing of these two phases is not well represented. In future work, these inaccuracies may be addressed by implementing a more sophisticated breakage scheme, where wave-induced flexion, collisions, and shearing due to ocean and atmosphere forcing are considered explicitly. These mechanisms are tied to the state of the pack as well as the external forcing, and may therefore evolve significantly during the time period considered here (Kohout & Meylan, 2008; Montiel & Squire, 2017; Williams et al., 2013). We also note that the small number of floes in our domain does not allow us to statistically establish the goodness of the power law fit and probe the detailed evolution of the modeled FSD against the observations. The validation is further hindered by the coarseness of MODIS imagery and the presence of clouds, which frequently mask the sea ice cover. Previous work has shown some promising results in the ability to distinguish various breakage mechanisms using high-resolution imagery (Hwang & Wang, 2022), and model them in a statistical sense (Boutin et al., 2020), but incorporating these dynamics into floe-resolving models remains a substantial task (Herman, 2017).

In our simulations, sea ice mass loss is dominated by vertical melt because the floes considered here have a large basal to peripheral area ratio. This differs from previous studies that consider smaller floes (several meters to a kilometer) and explicitly parametrize lateral melt (Boutin et al., 2020; Roach et al., 2018), and where basal and lateral melt contributions are comparable for mass loss. Nevertheless, here lateral melt plays a first-order role in controlling the size distribution of floes, even at scales larger than 2 km, consistent with the influence of ocean turbulence and sea ice motion in enhancing lateral heat transport toward floes (Gupta & Thompson, 2022; Horvat et al., 2016). The breakage of floes also increases their total peripheral area, thus potentially further enhancing susceptibility to lateral melt over the course of the simulations. The lateral melt rates inferred from our simulations (0.1–0.6 km d^{-1}) are substantially greater than estimates derived from models and observations of the Arctic (with highest values in the order of 1×10^{-3} km d^{-1}) (Maykut & Perovich, 1987; Steele, 1992; Tsamados et al., 2015). These differences likely stem from the fact that these past values were obtained in more compact regions of sea ice, where lateral ocean-induced melt occurs in constrained leads. In the MIZ, the presence of ocean eddies, higher ocean temperatures, and the greater motions of individual floes may substantially increase this lateral melt contribution. Obtaining estimates of lateral melt rates in the MIZ and across various floe sizes is thus essential to better constrain floe-aware models both here and in other studies.

The melt processes considered in our work are likely sensitive to several model idealizations. The present version of LS-ICE is coupled to a slab thermodynamic ocean, which does not capture the detailed evolution of the temperature profile underneath sea ice expected from cooling and freshening, or the dynamics of surface ocean currents, waves and tides. Floe velocity is prescribed from the domain-mean sea ice drift velocities obtained from observations, which does not include motions due to eddies or waves. Several important properties are fixed in time, such as the mixed layer depth, the ice albedo, and the insulating property of floes, which in reality evolve between spring and summer. Taken together, these idealizations may bias the partitioning between top, basal, and lateral sea ice melt inferred from our simulations. Here, we find that all three of these processes are important, thus

motivating the need to develop more sophisticated floe models coupled with a dynamic ocean to explore these dynamics in more detail.

A key question associated with floe-resolving models pertains to the minimum floe size that should be explicitly represented. Here, a natural threshold was the observable size from the satellite imagery used to validate the model. Unresolved floes comprised 44% of the total sea ice cover at the start of our simulations and were represented via a simple thickness distribution evolution. This representation has limitations and likely contributes to biases in the evolution of both the resolved and unresolved sea ice concentration. In the future, resolving a larger percentage of floes than in this work may be possible, but developing models that can blend unresolved and resolved floes will likely remain an important research priority.

The physical domain considered in this work is relatively small (400 km × 400 km), such that we do not fully capture the effects of larger-scale climate dynamics on sea ice evolution. We notably do not represent the advection of heat and sea ice within the region of interest, since we choose our domain to be doubly periodic. In our reference region within Baffin Bay, the domain-averaged sea ice velocities are small enough that ignoring net sea ice advection may be a reasonable assumption. However, it will be useful to evaluate this assumption more quantitatively and test the role of sea ice advection on the spring-to-summer evolution here and in other MIZs. Moreover, large-scale oceanic heat transport toward the poles is known to have a strong influence on sea ice (Aylmer et al., 2022, 2023; Decuypère et al., 2022; Steiner et al., 2021), and should therefore be explicitly considered in future work. Finally, the sensitivity analysis presented here may also vary in the context of Antarctic sea ice, where the bathymetric constraints, mean floe thickness, and snow fraction differ substantially from the Arctic.

5. Conclusions

This work uses a discrete element model of sea ice floes (LS-ICE) to investigate processes controlling the spring-to-summer decline of sea ice over marginal ice zones. The model is calibrated to a baseline simulation, which reproduces the statistical evolution of sea ice concentration within Baffin Bay in 2018, as observed from satellite imagery and reanalysis data (Moncada et al., 2023). In the parameter regime that best fits the observed sea ice concentration evolution, breakage and melt play a comparably important role in governing the mass decline of resolved floes (floe diameter > 2 km), with solar melt being more dominant than oceanic melt. The mass loss rate of these resolved floes is highly sensitive to the breakage rate B, and comparatively less sensitive to changes in the solar forcing S and the ice/ocean heat exchange coefficient q_v (Figure 4).

Signatures of the distinctive impacts of breakage and melt are evident in the time evolution of the FSD slope, which steepens due to breakage from the end of May to June, and shoals due to melt toward the end of June, consistent with previous observations (Denton & Timmermans, 2022; Hwang & Wang, 2022; Stern, Schweiger, Zhang, & Steele, 2018). A decomposition of the FSD evolution for the best-fit simulation reveals that the number loss of floes with sizes above a threshold $d_{bm} \sim 21$ km is dominated by breakage, whereas floes smaller than d_{bm} are regulated by melt. In sensitivity simulations, d_{bm} decreases for a higher breakage rate, but does not decrease below 10 km, due to the strong influence of solar melt.

The DEM and analysis framework employed here may help in the development of parameterizations of the FSD in coarse models with continuum representations of sea ice. Current schemes incorporate various parameterizations for processes such as the effects of waves on the fracturing of sea ice, lateral melt, growth, floe formation, welding, and wave radiation stress (Boutin et al., 2020; Roach et al., 2018, 2019). Implementations of these parameterizations in General Circulation Models (GCMs) have shown that floe-scale breakage and melt processes can have a substantial impact on the state of the pack in both hemispheres, notably via an enhanced ice-albedo feedback (Roach et al., 2018, 2019), and the impact of breakage on sea ice drift (Boutin et al., 2020). The model and observational results provided here may help further calibrate these dynamics, and allow GCMs to satisfy important bulk metrics such as the FSD evolution, the ratio of breakage to melt-induced sea ice changes, and the proportion of oceanic to solar melt, as inferred from increasingly detailed observations of the pack (Denton & Timmermans, 2022; Hoppmann et al., 2023; Horvat et al., 2019; Hwang & Wang, 2022; Wang et al., 2022).

The development of more advanced parameterizations for GCMs would likely benefit from DEMs with fewer idealizations than the one considered in this work. Important enhancements would likely include two-way

coupling with a dynamic ocean, physically based fracturing due to waves, collisions and drag forces, and more sophisticated thermodynamics that include snow evolution. The ability to explicitly represent a wider range of floe sizes and appropriately treating unresolved floes would also be important. This would also allow a more statistically robust estimates of the power law coefficient. These model developments will strongly rely on better observations of the pack, particularly sea ice imagery and upper-ocean properties at higher spatial and temporal resolution.

Our results highlight the importance of breakage for the springtime decay of sea ice. As Arctic sea ice thins and its strength is reduced, these dynamics may become increasingly relevant over a large portion of the seasonal cycle and for the longer-term evolution of the sea ice cover.

Conflict of Interest

The authors declare no conflicts of interest relevant to this study.

Data Availability Statement

MODIS images can be accessed from MODIS Science Team (2017). This study has been conducted using E.U. Copernicus Marine Service Information, specifically Arctic Ocean Physics Reanalysis, accessed from European Union-Copernicus Marine Service (2024) with ID ARCTIC_MULTIYEAR_PHY_002_003. In addition, ERA5 data are accessed from Hersbach et al. (2023) and NSIDC Polar Pathfinder Sea Ice Motion Vectors from Tschudi et al. (2019). Input and output data used for initializing simulations and generating results are available at Zenodo: https://doi.org/10.5281/zenodo.8237589. LS-ICE software for simulations is preserved at: https://zenodo.org/badge/latestdoi/676322610 and developed at GitHub: https://github.com/rmoncadalopez/LSICE.git.

Acknowledgments

R.M.L. and J.A.'s research was funded by the support of ARO Grant W911NF-19-1-0245 and the NSF Grant JEA. NSFCMMIECI-1-NSF.2033779. M.G. and A.F.T. were supported by award NSF-OCE 1829969 and the Office of Naval Research Multidisciplinary University Research Initiative (MURI) on Mathematics and Data Science for Physical Modeling and Prediction of Sea Ice, N00014-19-1-2421. Portions of the manuscript were performed under the auspices of the U.S. Department of Energy by Lawrence Livermore National Laboratory under Contract DE-AC52-07NA27344.

References

Andersson, T. R., Hosking, J. S., Pérez-Ortiz, M., Paige, B., Elliott, A., Russell, C., et al. (2021). Seasonal arctic sea ice forecasting with probabilistic deep learning. *Nature Communications*, *12*(1), 5124. https://doi.org/10.1038/s41467-021-25257-4

Aylmer, J., Ferreira, D., & Feltham, D. (2022). Different mechanisms of arctic and antarctic sea ice response to ocean heat transport. *Climate Dynamics*, *59*(1–2), 315–329. https://doi.org/10.1007/s00382-021-06131-x

Aylmer, J., Ferreira, D., & Feltham, D. (2023). Ocean heat transport regulates arctic sea ice loss. *Nature Portfolio*. https://doi.org/10.21203/rs.3.rs-3249087/v1

Bateson, A. W., Feltham, D. L., Schröder, D., Hosekova, L., Ridley, J. K., & Aksenov, Y. (2020). Impact of sea ice floe size distribution on seasonal fragmentation and melt of arctic sea ice. *The Cryosphere*, *14*(2), 403–428. https://doi.org/10.5194/tc-14-403-2020

Bateson, A. W., Feltham, D. L., Schröder, D., Wang, Y., Hwang, B., Ridley, J. K., & Aksenov, Y. (2022). Sea ice floe size: Its impact on pan-arctic and local ice mass and required model complexity. *The Cryosphere*, *16*(6), 2565–2593. https://doi.org/10.5194/tc-16-2565-2022

Blanchard-Wrigglesworth, E., Cullather, R., Wang, W., Zhang, J., & Bitz, C. (2015). Model forecast skill and sensitivity to initial conditions in the seasonal sea ice outlook. *Geophysical Research Letters*, *42*(19), 8042–8048. https://doi.org/10.1002/2015gl065860

Boutin, G., Lique, C., Ardhuin, F., Rousset, C., Talandier, C., Accensi, M., & Girard-Ardhuin, F. (2020). Towards a coupled model to investigate wave–sea ice interactions in the arctic marginal ice zone. *The Cryosphere*, *14*(2), 709–735. https://doi.org/10.5194/tc-14-709-2020

Brenner, S., Horvat, C., Hall, P., Lo Piccolo, A., Fox-Kemper, B., Labbé, S., & Dansereau, V. (2023). Scale-dependent air-sea exchange in the polar oceans: Floe-floe and floe-flow coupling in the generation of ice-ocean boundary layer turbulence. *Geophysical Research Letters*, *50*(23), e2023GL105703. https://doi.org/10.1029/2023GL105703

Clauset, A., Shalizi, C. R., & Newman, M. E. J. (2009). Power law distributions in empirical data. *SIAM Review*, *51*(4), 661–703. https://doi.org/10.48550/ARXIV.0706.1062

Decuypère, M., Tremblay, L. B., & Dufour, C. O. (2022). Impact of ocean heat transport on arctic sea ice variability in the gfdl cm2-o model suite. *Journal of Geophysical Research: Oceans*, *127*(3). https://doi.org/10.1029/2021jc017762

Dempsey, J. P., DeFranco, S. J., Blanchet, D., & Prodanovic, A. (1994). Mechanisms of fracture of sea ice. *Hydrotechnical Construction*, *28*(3), 164–168. https://doi.org/10.1007/bf01545933

Denton, A. A., & Timmermans, M.-L. (2022). Characterizing the sea-ice floe size distribution in the Canada basin from high-resolution optical satellite imagery. *The Cryosphere*, *16*(5), 1563–1578. https://doi.org/10.5194/tc-16-1563-2022

Deser, C., Tomas, R., Alexander, M., & Lawrence, D. (2010). The seasonal atmospheric response to projected arctic sea ice loss in the late twenty-first century. *Journal of Climate*, *23*(2), 333–351. https://doi.org/10.1175/2009jcli3053.1

Dinh, H., Giannakis, D., Slawinska, J., & Stadler, G. (2023). Phase-field models of floe fracture in sea ice. *The Cryosphere*, *17*(9), 3883–3893. https://doi.org/10.5194/tc-17-3883-2023

Dumont, D., Kohout, A., & Bertino, L. (2011). A wave-based model for the marginal ice zone including a floe breaking parameterization. *Journal of Geophysical Research*, *116*(C4), C04001. https://doi.org/10.1029/2010jc006682

European Union-Copernicus Marine Service. (2024). Baffin bay—arctic Ocean Physics reanalysis. *E.U. Copernicus Marine Service Information (CMEMS) Marine Data Store (MDS)*. https://doi.org/10.48670/moi-00007. Accessed on 12-08-2024.

Guemas, V., Blanchard-Wrigglesworth, E., Chevallier, M., Day, J. J., Déqué, M., Doblas-Reyes, F. J., et al. (2016). A review on arctic sea-ice predictability and prediction on seasonal to decadal time-scales. *Quarterly Journal of the Royal Meteorological Society*, *142*(695), 546–561. https://doi.org/10.1002/qj.2401

Gupta, M., Gürcan, E., & Thompson, A. F. (2024). Eddy-induced dispersion of sea ice floes at the marginal ice zone. *Geophysical Research Letters*, *51*(2), e2023GL105656. https://doi.org/10.1029/2023GL105656

Gupta, M., & Thompson, A. F. (2022). Regimes of sea-ice floe melt: Ice-ocean coupling at the submesoscales. *Journal of Geophysical Research: Oceans*, *127*(9), e2022JC018894. https://doi.org/10.1029/2022JC018894

Han, S., Yang, B., Yang, B., & Zhang, G. (2024). Numerical simulation of heterogeneous ice sheet-structure interaction based on cohesive element method. *Applied Ocean Research*, *145*, 103942. https://doi.org/10.1016/j.apor.2024.103942

Harmon, J. M., Arthur, D., & Andrade, J. E. (2020). Level set splitting in DEM for modeling breakage mechanics. *Computer Methods in Applied Mechanics and Engineering*, *365*, 112961. https://doi.org/10.1016/j.cma.2020.112961

Herman, A. (2013). Numerical modeling of force and contact networks in fragmented sea ice. *Annals of Glaciology*, *54*(62), 114–120. https://doi.org/10.3189/2013aog62a055

Herman, A. (2017). Wave-induced stress and breaking of sea ice in a coupled hydrodynamic discrete-element wave–ice model. *The Cryosphere*, *11*(6), 2711–2725. https://doi.org/10.5194/tc-11-2711-2017

Hersbach, H., Bell, B., Berrisford, P., Biavati, G., Horányi, A., Muñoz Sabater, J., et al. (2023). ERA5 hoaurly data on single levels from 1940 to present. *Copernicus Climate Change Service (C3S) Climate Data Store (CDS)*. https://doi.org/10.24381/cds.adbb2d47. Accessed on 12-08-2024.

Hoppmann, M., Allerholt, J., von Appen, W.-J., Cheng, B., Fer, I., Graupner, R., et al. (2023). Raw data files from autonomous instruments installed on Floe North in the marginal ice zone northwest of Svalbard in July 2022 as part of RV POLARSTERN expedition PS131 (ATWAICE) [Dataset]. *PANGAEA*. https://doi.org/10.1594/PANGAEA.963557

Horvat, C., Roach, L. A., Tilling, R., Bitz, C. M., Fox-Kemper, B., Guider, C., et al. (2019). Estimating the sea ice floe size distribution using satellite altimetry: Theory, climatology, and model comparison. *The Cryosphere*, *13*(11), 2869–2885. https://doi.org/10.5194/tc-13-2869-2019

Horvat, C., & Tziperman, E. (2015). A prognostic model of the sea-ice floe size and thickness distribution. *The Cryosphere*, *9*(6), 2119–2134. https://doi.org/10.5194/tc-9-2119-2015

Horvat, C., Tziperman, E., & Campin, J.-M. (2016). Interaction of sea ice floe size, ocean eddies, and sea ice melting. *Geophysical Research Letters*, *43*(15), 8083–8090. https://doi.org/10.1002/2016gl069742

Hwang, B., & Wang, Y. (2022). Multi-scale satellite observations of arctic sea ice: New insight into the life cycle of the floe size distribution. *Philosophical Transactions of the Royal Society A: Mathematical, Physical & Engineering Sciences*, *380*(2235). https://doi.org/10.1098/rsta.2021.0259

Hwang, B., Wilkinson, J., Maksym, T., Graber, H. C., Schweiger, A., Horvat, C., et al. (2017). Winter-to-summer transition of arctic sea ice breakup and floe size distribution in the beaufort sea. *Elementa: Science of the Anthropocene*, *5*. https://doi.org/10.1525/elementa.232

Kawamoto, R., Andò, E., Viggiani, G., & Andrade, J. E. (2016). Level set discrete element method for three-dimensional computations with triaxial case study. *Journal of the Mechanics and Physics of Solids*, *91*, 1–13. https://doi.org/10.1016/j.jmps.2016.02.021

Kawamoto, R., Andò, E., Viggiani, G., & Andrade, J. E. (2018). All you need is shape: Predicting shear banding in sand with LS-DEM. *Journal of the Mechanics and Physics of Solids*, *111*, 375–392. https://doi.org/10.1016/j.jmps.2017.10.003

Kohout, A. L., & Meylan, M. H. (2008). An elastic plate model for wave attenuation and ice floe breaking in the marginal ice zone. *Journal of Geophysical Research*, *113*(C9). https://doi.org/10.1029/2007jc004434

Kwok, R., Cunningham, G. F., & Pang, S. S. (2004). Fram strait sea ice outflow. *Journal of Geophysical Research*, *109*(C1). https://doi.org/10.1029/2003jc001785

Leppäranta, M. (2011). Free drift. *The Drift of Sea Ice*, 185–212. https://doi.org/10.1007/978-3-642-04683-4_6

Lopez-Acosta, R., Schodlok, M., & Wilhelmus, M. (2019). Ice floe tracker: An algorithm to automatically retrieve Lagrangian trajectories via feature matching from moderate-resolution visual imagery. *Remote Sensing of Environment*, *234*, 111406. https://doi.org/10.1016/j.rse.2019.111406

Lu, W., Lubbad, R., & Løset, S. (2015). In-plane fracture of an ice floe: A theoretical study on the splitting failure mode. *Cold Regions Science and Technology*, *110*, 77–101. https://doi.org/10.1016/j.coldregions.2014.11.007

Manucharyan, G. E., & Montemuro, B. P. (2022). SubZero: A sea ice model with an explicit representation of the floe life cycle. *Journal of Advances in Modeling Earth Systems*, *14*(12). https://doi.org/10.1029/2022ms003247

Maykut, G. A., & Perovich, D. K. (1987). The role of shortwave radiation in the summer decay of a sea ice cover. *Journal of Geophysical Research*, *92*(C7), 7032–7044. https://doi.org/10.1029/jc092ic07p07032

McPhee, M. G. (1992). Turbulent heat flux in the upper ocean under sea ice. *Journal of Geophysical Research*, *97*(C4), 5365–5379. https://doi.org/10.1029/92jc00239

Min, C., Yang, Q., Mu, L., Kauker, F., & Ricker, R. (2021). Ensemble-based estimation of sea-ice volume variations in the baffin bay. *The Cryosphere*, *15*(1), 169–181. https://doi.org/10.5194/tc-15-169-2021

MODIS Science Team. (2017). Modis/terra calibrated radiances 5-min l1b swath 1km [Dataset]. *NASA LANCE MODIS at the MODAPS*. https://doi.org/10.5067/MODIS/MOD021KM.NRT.061

Moncada, R., Gupta, M., Thompson, A., & Andrade, J. (2023). Level set discrete element method for modeling sea ice floes. *Computer Methods in Applied Mechanics and Engineering*, *406*, 115891. https://doi.org/10.1016/j.cma.2023.115891

Montiel, F., & Squire, V. A. (2017). Modelling wave-induced sea ice break-up in the marginal ice zone. *Proceedings of the Royal Society A: Mathematical, Physical and Engineering Sciences*, *473*(2206), 20170258. https://doi.org/10.1098/rspa.2017.0258

Moon, T. A. M. L. D., & Thoman, R. (2021). Noaa arctic report card 2021 executive summary. *Arctic Report Card*. https://doi.org/10.25923/5S0F-5163

Olonscheck, D., Mauritsen, T., & Notz, D. (2019). Arctic sea-ice variability is primarily driven by atmospheric temperature fluctuations. *Nature Geoscience*, *12*(6), 430–434. https://doi.org/10.1038/s41561-019-0363-1

Perovich, D. K., & Jones, K. F. (2014). The seasonal evolution of sea ice floe size distribution. *Journal of Geophysical Research: Oceans*, *119*(12), 8767–8777. https://doi.org/10.1002/2014jc010136

Ren, H., Zhang, C., & Zhao, X. (2021). Numerical simulations on the fracture of a sea ice floe induced by waves. *Applied Ocean Research*, *108*, 102527. https://doi.org/10.1016/j.apor.2021.102527

Roach, L. A., Bitz, C. M., Horvat, C., & Dean, S. M. (2019). Advances in modeling interactions between sea ice and ocean surface waves. *Journal of Advances in Modeling Earth Systems*, *11*(12), 4167–4181. https://doi.org/10.1029/2019ms001836

Roach, L. A., Horvat, C., Dean, S. M., & Bitz, C. M. (2018). An emergent sea ice floe size distribution in a global coupled ocean-sea ice model. *Journal of Geophysical Research: Oceans*, *123*(6), 4322–4337. https://doi.org/10.1029/2017jc013692

Rothrock, D. A., & Thorndike, A. S. (1984). Measuring the sea ice floe size distribution. *Journal of Geophysical Research*, *89*(C4), 6477–6486. https://doi.org/10.1029/jc089ic04p06477

Serreze, M. C., & Stroeve, J. (2015). Arctic sea ice trends, variability and implications for seasonal ice forecasting. *Philosophical Transactions of the Royal Society A: Mathematical, Physical & Engineering Sciences*, *373*(2045), 20140159. https://doi.org/10.1098/rsta.2014.0159

Steele, M. (1992). Sea ice melting and floe geometry in a simple ice-ocean model. *Journal of Geophysical Research*, *97*(C11), 17729–17738. https://doi.org/10.1029/92jc01755

Steiner, N. S., Bowman, J., Campbell, K., Chierici, M., Eronen-Rasimus, E., Falardeau, M., et al. (2021). Climate change impacts on sea-ice ecosystems and associated ecosystem services. *Elementa: Science of the Anthropocene*, *9*(1). https://doi.org/10.1525/elementa.2021.00007

Stern, H. L., Schweiger, A. J., Stark, M., Zhang, J., Steele, M., & Hwang, B. (2018a). Seasonal evolution of the sea-ice floe size distribution in the beaufort and chukchi seas. *Elementa: Science of the Anthropocene*, *6*. https://doi.org/10.1525/elementa.305

Stern, H. L., Schweiger, A. J., Zhang, J., & Steele, M. (2018b). On reconciling disparate studies of the sea-ice floe size distribution. *Elementa: Science of the Anthropocene*, *6*. https://doi.org/10.1525/elementa.304

Stroeve, J. C., Markus, T., Boisvert, L., Miller, J., & Barrett, A. (2014). Changes in arctic melt season and implications for sea ice loss. *Geophysical Research Letters*, *41*(4), 1216–1225. https://doi.org/10.1002/2013gl058951

Timco, G., & Weeks, W. (2010). A review of the engineering properties of sea ice. *Cold Regions Science and Technology*, *60*(2), 107–129. https://doi.org/10.1016/j.coldregions.2009.10.003

Tooth, M., & Tschudi, M. (2018). Investigating arctic sea ice survivability in the beaufort sea. *Remote Sensing*, *10*(2), 267. https://doi.org/10.3390/rs10020267

Tsamados, M., Feltham, D., Petty, A., Schroeder, D., & Flocco, D. (2015). Processes controlling surface, bottom and lateral melt of arctic sea ice in a state of the art sea ice model. *Philosophical Transactions of the Royal Society A: Mathematical, Physical & Engineering Sciences*, *373*(2052), 20140167. https://doi.org/10.1098/rsta.2014.0167

Tschudi, M., Meier, W. N., Stewart, J. S., Fowler, C., & Maslanik, J. (2019). *Polar pathfinder daily 25 km ease-grid sea ice motion vectors*. NASA National Snow and Ice Data Center Distributed Active Archive Center. https://doi.org/10.5067/INAWUWO7QH7B

Wang, Y., Hwang, B., Bateson, A. W., Aksenov, Y., & Horvat, C. (2022). Summer sea ice floe size distribution in the arctic: High-resolution optical satellite imagery and model evaluation. *The Cryosphere*. https://doi.org/10.5194/tc-2022-130

Wei, J., Zhang, X., & Wang, Z. (2019). Reexamination of fram strait sea ice export and its role in recently accelerated arctic sea ice retreat. *Climate Dynamics*, *53*(3–4), 1823–1841. https://doi.org/10.1007/s00382-019-04741-0

Weiss, J., & Marsan, D. (2004). Scale properties of sea ice deformation and fracturing. *Comptes Rendus Physique*, *5*(7), 735–751. https://doi.org/10.1016/j.crhy.2004.09.005

West, B., O'Connor, D., Parno, M., Krackow, M., & Polashenski, C. (2022). Bonded discrete element simulations of sea ice with non-local failure: Applications to nares strait. *Journal of Advances in Modeling Earth Systems*, *14*(6). https://doi.org/10.1029/2021ms002614

Williams, T. D., Bennetts, L. G., Squire, V. A., Dumont, D., & Bertino, L. (2013). Wave–ice interactions in the marginal ice zone. part 1: Theoretical foundations. *Ocean Modelling*, *71*, 81–91. https://doi.org/10.1016/j.ocemod.2013.05.010